Waste Management 218 (2026) 115518

Contents lists available at ScienceDirect

Waste Management

journal homepage: www.elsevier.com/locate/wasman

Research Paper

Thermal decomposition pathways of extracellular polymeric substances recovered from wastewater sludge using TG-FTIR with Gaussian deconvolution and 2D-COS analysis

Tan Minh Le [a,b], Yuemei Lin [c,*], Wei-Qin Zhuang [d], Mark C.M. van Loosdrecht [c], Krishnan Jayaraman [a,b], Nam Kyeun Kim [a,b,*]

[a] Centre for Advanced Materials Manufacturing and Design, University of Auckland, Auckland 1023, New Zealand
[b] Department of Mechanical and Mechatronics Engineering, University of Auckland, Auckland 1010, New Zealand
[c] Department of Biotechnology, Delft University of Technology, Delft 2629HZ, the Netherlands
[d] Department of Civil and Environmental Engineering, University of Auckland, Auckland 1010, New Zealand

ARTICLE INFO

Keywords:
Extracellular polymeric substances
Gaussian deconvolution
2D-COS
Char formation
Pyrolysis
Activation energy

ABSTRACT

The current research attempts to elucidate fundamental mechanistic correlation between the complex chemical architecture of wastewater-derived biopolymers – EPS (extracellular polymeric substances) and their inherent thermal properties for fire-safety applications. By integrating thermogravimetric-infrared spectroscopy with two-dimensional correlation spectroscopy, we resolve intricate mass-loss profiles into three pseudo-components (PCs), each characterised by kinetic signatures and functional group transformations. PC1 (150–350 °C, activation energy (AE) = 140–150 kJ/mol), is primarily governed by the degradation of polysaccharides and release of early-stage volatiles (H_2O, CO_2, CH_4, NH_3, and HNCO). PC2 (210–450 °C, AE = 160–175 kJ/mol), represent the transition stage dominated by proteinaceous and lipid cross-linking, which produces nitrogenous species essential for promoting condensed-phase char development. PC3 (290–600 °C, AE > 180 kJ/mol) corresponds to the decomposition of humic-like substances and subsequent aromatic condensation of stable residues. Furthermore, comparative analysis reveals that EPS extracted from activated sludge exhibits higher thermal stability and a significantly increased char yield (33.5 %) than aerobic counterpart, attributed to higher AE during the middle decomposition stage. The persistent detection of C-O-C/P–O–C and aromatic C=C vibrations up to 700 °C confirms the formation of a phosphorus-rich aromatic char structure. This multi-dimensional analytical framework moves beyond conventional TG-based pseudo-component fitting, providing high resolution interpretation of the sequential evolution of volatile species and early-stage charring mechanisms of EPS.

1. Introduction

The large volumes of wastewater sludge generated from wastewater treatment plants poses challenges to water utilities worldwide in terms of sludge management (Nkuna et al., 2024). Extracellular polymeric substances (EPS) are an emerging material derived from wastewater sludge with various potential applications in agriculture (Shi et al., 2023), construction (Lin et al., 2015), and as flame retardant (Kim et al., 2023). Recovery of EPS from wastewater sludge has been demonstrated as a sustainable pathway for sludge management (De Bruin et al., 2026; Zheng et al., 2024). EPS, a high molecular weight biopolymer (M_w > 10,000 Da) (Morgan et al., 1990), is produced by the microorganisms that clean the wastewater. EPS contains different polymers, such as polysaccharides, proteins, lipids, nucleic acids, and humic-like substances (Felz et al., 2016). The characteristic properties of EPS are influenced by various factors including the source of sludge, environmental conditions, and extraction methods (Chen et al., 2022). Therefore, determining the composition and properties of EPS is a critical prerequisite before pursuing any specific application. Although many analysis methods for characterising EPS have been developed over the decades, the standardised method for EPS extraction and analysis is still under development, resulting in inconsistent or incomparable data

* Corresponding authors at: Department of Biotechnology, Delft University of Technology, Delft 2629HZ, The Netherlands (Y. Lin). Centre for Advanced Materials Manufacturing and Design, University of Auckland, B903, 262 Khyber Pass Road, Auckland 1023, New Zealand (N. K. Kim).
E-mail addresses: yuemei.lin@tudelft.nl (Y. Lin), nam.kim@auckland.ac.nz (N.K. Kim).

https://doi.org/10.1016/j.wasman.2026.115518
Received 25 November 2025; Received in revised form 26 March 2026; Accepted 7 April 2026
Available online 17 April 2026

across studies (Hamed et al., 2025).

Colourimetric methods are common techniques used to estimate EPS composition. For example, the phenol–sulfuric acid method for quantifying polysaccharide content (DuBois et al., 1956), and the modified Lowry method for analysing protein and humic-like substance contents (Frølund et al., 1996). However, these methods measure the EPS composition by comparing it with reference samples, which leads to inconsistent results and reduced reproducibility (Felz et al., 2019). To overcome experimental biases associated with colourimetric techniques, advanced techniques, such as Fourier-Transform Infrared Spectroscopy (FT-IR), Gas Chromatography (GC), High-Performance Liquid Chromatography, and Mass Spectrometry (MS), can be used to ensure reliable results and facilitate effective cross-referencing and comparison. Among these, FTIR and thermogravimetric analysis (TGA) are particularly outstanding methods because it is rapid, simple, and capable of providing chemical and thermal properties of EPS. For instance, de Bruin et al. (De Bruin et al., 2026) used FTIR to distinguish the composition of EPS extracted from activated sludge around the world. Shi et al. (Shi et al., 2023) demonstrated that using FTIR can clarify the differences in compositional blocks fractioning from EPS recovered from activated sludge. Campo et al. (Campo et al., 2022) determined the thermal properties of the soluble fraction of EPS from granular sludge and EPS-based hydrogel by using TGA. However, due to the complex composition of EPS, the derivative thermogravimetric (DTG) dataset curves from EPS are typically broad and featureless, making it challenging to resolve overlapping thermal reactions and attribute decomposition contributions to specific components. To overcome this problem, chemometrics can be used to enrich the information for TGA. Gaussian deconvolution has proven effective in distinguishing individual DTG peaks, enabling the identification of thermal parameters and pyrolysis characteristics of different components. For example, Li et al. (Li et al., 2019) employed TGA combined with Gaussian deconvolution to compare the thermal properties of granular and flocculated sludge. Their results showed that the Gaussian model effectively fitted the DTG data from these sludges and separated the decomposition profiles into three pseudo-components. Recently, Le et al. (2025) also investigated the thermal stability of EPS extracted using different methods by combining TGA with Gaussian deconvolution. They found that the DTG profiles of EPS obtained from various extraction techniques can also be deconvoluted into three pseudo-components, potentially corresponding to polysaccharides, proteins, humic-like substances, and lipids. However, the main limitation of these studies lies in the interpretation of pseudo-components solely based on literature data and activation energy estimation, without direct evidence of chemical transformations. This restricts the practical application of the findings. To overcome this limitation, in-situ monitoring of both the chemical and thermal changes during EPS decomposition can provide more reliable insights into its decomposition mechanisms and structure–property relationships.

In practice, thermogravimetry can be coupled with Fourier transform infrared spectroscopy (TG–FTIR), providing a powerful, rapid, and sensitive in-situ method for identifying gaseous species released during pyrolysis. By correlating thermograms with spectrograms, TG–FTIR not only validates mass loss data but also reveals the evolution of volatile products. Furthermore, FTIR can monitor changes in functional groups of solid residues, providing deeper insight into the thermal decomposition pathways. Song et al. (Song et al., 2019) demonstrated that Gaussian deconvolution could resolve functional group contributions during biomass pyrolysis by analysing spectra of residual char. Moreover, FTIR datasets collected at different temperatures can be utilised to investigate molecular structure evolution during pyrolysis through two-dimensional correlation spectroscopy (2D-COS) analysis (Park et al., 2018). Ni et al. (Ni et al., 2023) applied 2D-COS to elucidate the gas-release mechanisms during the co-decomposition of cellulose and coal slime. Uchimiya et al. (Uchimiya et al., 2018) further demonstrated that FTIR-2D-COS is a powerful tool for understanding char formation and surface functionality development in biochar. Several studies have used in-situ TG-FTIR to understand the properties of biopolymers, predict their chemical properties, and determine the kinetic mechanisms of materials (Jia et al., 2024; Lin et al., 2017; Wang et al., 2022). However, to the best of our knowledge, no studies have specifically elucidated the decomposition mechanisms and structure–property relationships of EPS recovered from sludge (Song et al., 2026).

Since thermal properties are among the most important characteristics of EPS — governing their thermal stability and decomposition behaviour — they play a pivotal role in polymer processing, conversion into value-added products, as well as various applications. In particular, understanding thermal decomposition is a fundamental step in evaluating flame-retardant potential, since key mechanisms, such as suppression of heat transfer, non-volatile gas release and char formation, are governed by degradation pathways. Thermal decomposition parameters including gas evolution profile, residual char yield and mass loss rate are widely used as indicators of flame-retardant efficiency. In this study, the thermal decomposition behaviours of EPS recovered from wastewater sludge were investigated using TG–FTIR in combination with Gaussian deconvolution and 2D-COS analysis. EPS were extracted from aerobic activated sludge and anaerobic digested sludge using alkaline-acid method. The TGA/DTG data, together with deconvolution analysis, were employed to elucidate the thermal decomposition kinetics and reaction parameters of the pseudo-components (PCs) of EPS. The dynamic evolution and chemical transformations of gaseous species during EPS pyrolysis were monitored in-situ by TG–FTIR. By integrating TG–FTIR with Gaussian deconvolution, the chemical constituents corresponding to each PC were identified, enabling the proposed decomposition pathways of EPS to be established for the first time. The char residues obtained from TGA were analysed by FTIR and 2D-COS to verify the proposed decomposition mechanisms and evaluate the char formation behaviour. Overall, the findings provide a systematic understanding of EPS pyrolysis, offering new tools to evaluate the thermal properties of EPS and to manage wastewater sludge for the development of EPS-derived flame-retardant materials.

2. Materials and methods

2.1. Materials

The raw sludge samples, including aerobic activated sludge (AS) and anaerobic digested sludge (BS), were collected from the Māngere wastewater treatment plant, Watercare Services, Auckland, New Zealand. The EPS was extracted using the alkaline-acid method as described by Le et al. (2025). First, 3 g of sludge was soaked with 1 % (w/v) NaOH solution at 80 °C for 30 min under continuous stirring at 250 rpm. The mixture was then centrifuged at 7000 rpm, and the supernatant was collected. The pH of the supernatant was subsequently adjusted to pH 2 using 1 M HCl to precipitate the EPS. The precipitated EPS was recovered by centrifugation at 7000 rpm. Finally, the EPS was dried at 80 °C

Table 1
Chemical compositions of EPS from different types of sludge.

	Abbreviation	VS%	PN	PS	HS
		%	mg/g EPS	mg/g EPS	mg/g EPS
EPS from activated sludge	AS	74.36 ± 4.08	189.38 ± 4.1	58.26 ± 2.02	342.36 ± 2.72
EPS from digested sludge	BS	80.03 ± 0.68	92.06 ± 5.36	79.90 ± 1.14	604.31 ± 5.99

*VS: volatile solids, PN: proteins, determined by modified Lowry method (Frølund et al., 1996) with albumin as a standard, HS: humic-like substances determined by modified Lowry method (Frølund et al., 1996) with humic acid as the standard, and PS: polysaccharides using the phenol–sulfuric acid method (DuBois et al., 1956) with D-glucose as the standard.

overnight and stored in a sealed bottle at room temperature for further use. The general composition of extracted EPS is shown in Table 1.

2.2. Thermogravimetric – Fourier transform infrared Spectrometry analysis

The pyrolysis was conducted under an inert gas atmosphere (N_2, 50 mL/min flow rate) using a TGA (Q5000, TA Instruments, USA) with heating rates of 10, 20, and 30 °C/min in a temperature range of 100 – 700 °C. The sample weight was maintained at around 10–15 mg to minimise the effects of noise and particle size. All experiments were conducted with at least three replications to ensure the standard deviation of the TG curve was less than 5 %.

On-line TG-FTIR: The pyrolytic gases released from the TGA equipment during measurement at a heating rate of 30 °C/min were swept into the FTIR (Perseus, alpha II FT-IR, Bruker, Australia). The absorbance of pyrolytic gases was measured with a scanning range of 4000–400 cm^{-1}, every 10 °C for each sample. The transfer line was maintained at 200 °C to prevent gas condensation.

Off-line TG-FTIR: The char residues obtained from TGA measurements at temperatures ranging from 100 °C to 700 °C, in 50 °C intervals, were collected for further analysis. These residues were subsequently characterised using attenuated total reflectance Fourier-transform infrared spectroscopy (ATR-FTIR; Nicolet iS50, Thermo Fisher Scientific, USA) over a wavenumber range of 4000–400 cm^{-1}.

2.3. Data analysis

2.3.1. Gaussian deconvolution

The Gaussian equation (Eq. (1) used for deconvolution is described as follows:

$$y = y_0 + \frac{Ae^{\frac{-4\ln(2)(x-x_c)^2}{w^2}}}{w\sqrt{\frac{\pi}{4\ln(2)}}} \tag{1}$$

where: y and y_0 are predicted and experimental values, respectively. A is the area under the curve. x, x_c and w are the temperature, a peak temperature, and full width at half maximum, respectively.

In this study, the data pre-processing and deconvolution method were conducted using the Peak Analyser function in Origin Lab 2025 software. The DTG curves of each EPS sample were deconvoluted into three distinct pseudo-components (PCs). The number of peaks was determined by identifying observable maxima, shoulders and inflection points in the experimental DTG and Gram-Schmidt (GS) profiles (Tobar et al., 2023). To ensure a physically meaning model, additional peaks were introduced only if they corresponded to documented thermal degradation events and provides statistically significant improvement to the fit. To avoid overfitting, the parsimony principle was applied, selecting the minimum number of peaks required to achieve the coefficient of determination, Eq. (2) ($R^2 > 0.99$) and a minimised Root Mean Square Error (RMSE), Eq. (3) (Erickson et al., 2018).

$$R^2 = 1 - \frac{\sum (y_i - \hat{y}_i)^2}{\sum (y_i - \bar{y})^2} \tag{2}$$

$$RMSE = \sqrt{\frac{1}{n}\sum_{i=1}^{n} (\hat{y}_i - y_i)^2} \tag{3}$$

where $\hat{y}_i$ is the predicted values, y_i is the experimental values, $\bar{y}$ is the mean value, n is the number of data points. The fitting model was considered to have robustness accuracy when the R^2 values were close to 1 and the RMSE was lower than 0.1 (Gan et al., 2022).

2.3.2. Two-dimensional correlation of spectroscopy (2D-COS)

In this study, two 2D-COS methods are used, including homogeneous (or generalised) and heterogeneous 2D-COS in the temperature range of 150–700 °C using Origin Lab software (USA). The values of FTIR absorbance (x) at different perturbations of temperature (T) were collected. The variation of dynamic spectrum, [$\tilde{y}(x, T)$], and the changes of dynamic spectrum following T, [$y(x, T)$], are functionalised as Eq. (4).

$$\tilde{y}(x,T) = \begin{Bmatrix} y(x,T) - \bar{y}(x) & for\ T_{\min} \leqslant T \leqslant T_{\max} \\ 0 & otherwise \end{Bmatrix} \tag{4}$$

where $\bar{y}(x) = \frac{1}{T_{max}-T_{min}}\int_{T_{min}}^{T_{max}} y(x,T)dT$ is the reference spectrum. In this study, we selected the average spectrum as a reference (Lasch and Noda, 2019).

In the homogeneous 2D-COS analysis, the synchronous signal of each sample is calculated using Eq. (5). The synchronous spectra indicate that the auto-peaks, which are sensitive to perturbation changes, appear at diagonal positions. At the same time, the symmetrical cross-peaks, representing the intensity changes of two wavenumbers, are in the off-diagonal position.

Homogeneous synchronous signal:

$$\varphi(x_1, x_2) = \frac{1}{T_{max} - T_{min}} \int_{T_{min}}^{T_{max}} \tilde{y}(x_1, T) \cdot \tilde{y}(x_2, T) dT \tag{5}$$

The heterogeneous 2D-COS was used to determine the possible correlation between gas and condensed phases, thus clarifying the pyrolysis mechanism of EPS. The dynamic spectrum of char and gas at different probes is a function of $\tilde{A}(x_1, T)$ and $\tilde{B}(x_2, T)$, respectively. The heterogeneous synchronous signals are calculated as follows:

$$\varphi(x_1, x_2)^{hetero} = \frac{1}{T_{max} - T_{min}} \int_{T}^{T_{max}} \tilde{A}(x_1, T) \cdot \tilde{B}(x_2, T) dT \tag{6}$$

2.4. Determination of activation energy

The apparent activation energy (AE), depending on the conversion rates (α), Eq. (7), of each PC, was estimated using Flynn–Wall–Ozawa (FWO) and Kissinger-Akahira-Sunose (KAS) methods, as expressed in Eqs. (8) and (9), respectively:

$$\text{Conversion rate}: \ \alpha = \frac{W_o - W_i}{W_o - W_f} \tag{7}$$

$$\text{FWOmethod}: \ln\beta = c - 1.052\frac{E}{RT} \tag{8}$$

$$\text{KASmethod}: \ln\left(\frac{\beta}{T^2}\right) = \ln\left(\frac{AR}{Eg(\alpha)}\right) - \frac{E}{RT} \tag{9}$$

where E is the apparent activation energy (kJ/mol), β is the heating rate (^oC/min), R is the ideal gas constant (8.314 J/mol·K), and T is the absolute temperature (K). A is the pre-exponential factor (s^{-1}), and g(α) is a function of the conversion rate (α). W_i, W_o, and W_f (mg) represent the weights of the sample at i, initial, and final temperatures, respectively.

3. Results

3.1. Thermal decomposition profiles of EPS

Thermogravimetric and Gram-Schmidt (GS) curves of EPS pyrolysis from different sources are presented in Fig. 1. The TGA results for both samples reveal three distinct stages of thermal degradation: dehydration, devolatilisation, and mineral decomposition. The first stage occurs between room temperature and 150 °C, corresponding to the removal of bound water. The total mass loss associated with moisture evaporation is 2.37 wt% of the initial mass for AS and 0.53 wt% for BS. The second stage, spanning 150–550 °C, accounts for the most significant proportion of mass loss, with 61.52 wt% for AS and 64.87 wt% for BS. This

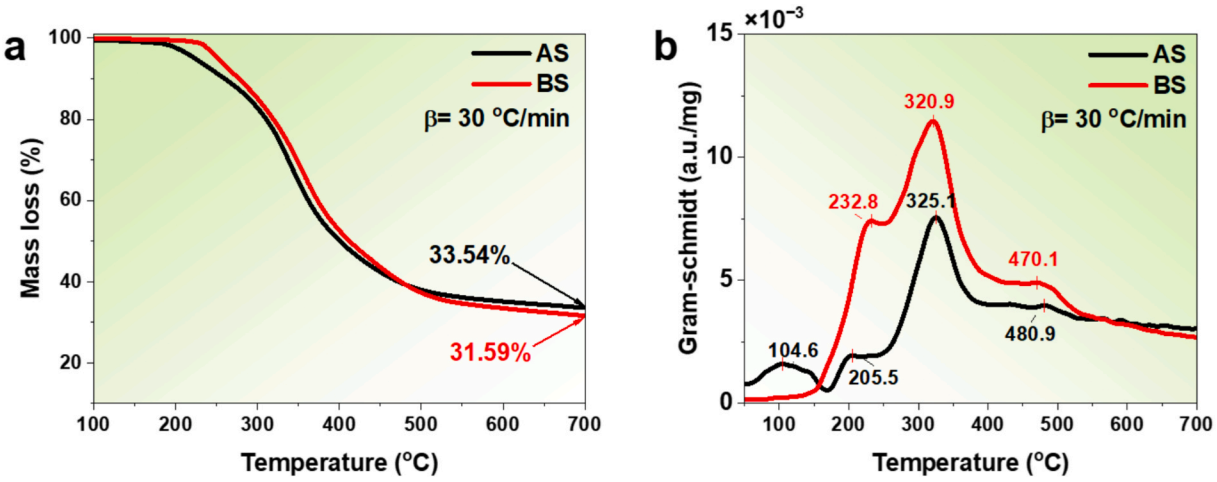

Fig. 1. The TGA (a) and Gram-Schmidt curves (b) of EPS from aerobic and anaerobic digested sludge at β = 30 °C/min.

stage is dominated by extensive devolatilisation, reflecting the thermal decomposition of major EPS constituents, including lipids, polysaccharides, proteins, humic-like substances, and other molecular fractions (Le et al., 2025a). The third stage (550–700 °C) corresponds to the steady pyrolysis phase, primarily associated with the decomposition of carboxylic acid salts and the progressive degradation of carbonaceous residues, contributing an additional mass loss of approximately 13.47 wt %. Overall, the final residual mass of AS is 33.54 wt%, slightly higher than that of BS (31.59 wt%).

The GS curve provides a quantitative representation of FTIR spectroscopy, where the ion current intensity varies with time in proportion to the concentration of gaseous volatiles released during pyrolysis (Zeng et al., 2024). In the GS curves (Fig. 1b), a distinct peak at 104 °C in the AS sample indicates a higher moisture and volatile content than in the BS sample. Between 150 °C and 550 °C, devolatilisation occurs as a result of the decomposition of various EPS constituents, which is consistent with TGA results. Notably, the BS sample from anaerobic digested sludge releases a greater quantity of gases than AS in this region, suggesting that BS has a higher decomposition rate than AS. Beyond 500 °C, the GS curve attains a steady state, indicating the completion of the decomposition process. Interestingly, the shapes of the TGA and GS curves for both EPS samples are similar, suggesting that they likely follow a similar decomposition mechanism.

3.2. DTG and its deconvolution results

The DTG curve and its Gaussian deconvolution results of EPS are shown in Fig. S1 (Supplementary data). The shapes of the DTG curves remain unchanged at various heating rates for both types of EPS, indicating that the reaction mechanisms of these EPS are not influenced by changes in heating rates (Gesese et al., 2024). However, the variation in the DTG curves of the EPS shows the differences in their thermal characteristics. After applying Gaussian deconvolution, the DTG signals of both AS and BS in the temperature range of 100 °C to 700 °C are resolved into three distinct peaks, corresponding to three pseudo-components (PCs). The deconvolution results exhibit RMSE values of 0.01–0.013 and R^2 values of 0.9900–0.9968, indicating an excellent fit between the model and the experimental data. Therefore, the deconvolution results can reliably be used to visualise and interpret the thermal properties of both EPS samples.

The properties of each PC from AS and BS at different heating rates are summarised in Table 2. In both samples, the DTG curves can be deconvoluted into three main peaks (PC1, PC2, and PC3), which are centred within temperature ranges of approximately 120–358 °C, 227–454 °C, and 289–596 °C for AS, and 160–349 °C, 215–477 °C, and 284–593 °C for BS, respectively. Despite slight differences in their temperature ranges, these peaks are clearly distinguishable in both cases, indicating that the decomposition of EPS from different sludge sources follows similar thermal stages. The weight loss of PC2 in both samples accounts for 47.23–60.23 %, whereas the weight loss of PC1 and PC3 each contributes around 20 % of the total mass loss. Also, the peak decomposition rate of PC2 is significantly higher than that of other PCs, suggesting that PC2 can represent for the main decomposition of EPS.

Table 2
Properties of Pseudo-components at different heating rates of AS and BS.

β (°C/min)	Pseudo-component 1 (PC1)				Pseudo-component 2 (PC2)				Pseudo-component 3 (PC3)			
	$T_{i\text{-}f}$ (°C)	R_{p1} (%/°C)	T_p (°C)	ΔW_1 (%)	$T_{i\text{-}f}$ (°C)	R_{p2} (%/°C)	T_{p2} (°C)	ΔW_2 (%)	$T_{i\text{-}f}$ (°C)	R_{p3} (%/°C)	T_{p3} (°C)	ΔW_3 (%)
EPS from aerobic activated sludge (AS)												
10	120 – 352	0.14	229.84	23.97	227 – 434	0.38	323.60	47.23	299 – 572	0.13	413.58	28.80
20	129 – 352	0.14	240.46	21.93	233 – 440	0.39	336.67	50.26	289 – 572	0.13	426.02	27.81
30	123 – 358	0.13	245.65	21.95	233 – 454	0.39	341.99	55.78	295 – 596	0.12	438.40	22.26
EPS from anaerobic digested sludge (BS)												
10	160—345	0.19	244.11	21.02	216 – 450	0.38	328.59	54.11	291 – 565	0.13	433.02	24.87
20	163—349	0.20	255.44	21.11	215—466	0.39	340.66	53.00	284 – 572	0.14	4441.03	25.88
30	168—349	0.18	258.07	16.61	222—477	0.38	348.49	60.23	291 – 593	0.13	454.72	23.16

$T_{i\text{-}f}$ (°C): decomposition temperature range of each PC.
R_p (%/°C): peak decomposition rate of PC.
T_p (°C): temperature of peak decomposition rate.
ΔW (%): total mass loss of PC (peak area of PC).

3.3. Activation energy of pseudo-components

The apparent AE values of three PCs of AS and BS in the α range from 0.1 to 0.9, with increments of 0.05 using the FWO and KAS methods, are shown in Fig. S2a-b. The fitting lines of each regression are presented in Fig. S3. The R^2 of all fitting lines ranges from 0.8805 to 0.9998, implying the reliability of this calculation (Table S1). In the case of AS, the AE distributions of PC1, PC2, and PC3 are in a range of 105.90 – 180.88 kJ/mol, 149.69 – 245.63 kJ/mol, and 91.70 – 323.31 kJ/mol, respectively. In comparison, the AE distributions of PC1, PC2, and PC3 from BS are in ranges of 104.24 – 191.22 kJ/mol, 131.28 – 176.30 kJ/mol, and 135.05 – 233.36 kJ/mol, respectively. Surprisingly, the trend of apparent AE following the conversion rates in the decomposition of BS is almost similar to that of AS. Herein, the AE of PC1 and PC3 tends to increase with elevated temperatures, whereas the AE of PC2 decreases with rising temperatures. This suggests that under temperature exposure, PC1 and PC3 are decomposed to produce a more stable structure, which requires higher energy to break down. On the other hand, the PC2 is essentially degraded into less thermally stable structures or compounds (lower AE), which are readily decomposed as the temperature increases (Vyazovkin, 2025).

For PC1, the average AE of AS (142.4 kJ/mol) is lower than that of BS (151.9 kJ/mol), consistent with the earlier onset temperature and higher gas-release intensity observed in Fig. 1. This lower AE implies that the initial degradation of AS requires less energy to initiate. While the average AE value of PC2-AS (172.8 kJ/mol) is higher than that of PC2-BS (161.0 kJ/mol), this suggests that PC2 from AS exhibits higher thermal stability. In contrast, the highest average AE values were observed for PC3, implying that this stage involves the degradation of more thermally stable compounds and contributes to the formation of a condensed char structure. Notably, the difference between AE values during the decomposition process is more than 20 %, indicating that the decomposition of each PC can be regarded as more than one reaction or component (Vyazovkin et al., 2011). AE is considered an important kinetic parameter for evaluating the thermal stability of materials and is often used as an indirect indicator of flame-retardant potential (Mu et al., 2022). A higher AE corresponds to a greater energy barrier for thermal decomposition, which can retard the pyrolysis rate and delay the release of combustible volatiles (Zhu et al., 2021). Liang et al. (Liang et al., 2021) compared the flame-retardant performance of two lignin–epoxy composites and reported that the alkaline lignin–epoxy system, which exhibited lower activation energy, showed higher total heat release (THR) and peak heat release rate compared to the lignin@ammonium polyphosphate–epoxy composite. These findings suggest that materials with higher activation energy may exhibit improved resistance to rapid thermal degradation.

In this case, the deconvolution should be reconstructed to determine more PCs to reduce the overlapping reaction. However, based on some previous studies, most of the studies have accepted the presence of three PCs in lignocellulosic and non-lignocellulosic biomass. For example, Thipkhunthod et al. (Thipkhunthod et al., 2007) demonstrated that the thermal decomposition of sludge can be reasonably divided into three PCs, as sludge typically contains a variety of complex and heterogeneous compounds, such as polysaccharides composed of sugars and peptides (Li et al., 2024). In agreement, Li et al., (2024) reported that the decomposition behaviours of both flocculated and granular sludges can be deconvoluted into three distinct PC peaks. Considering that EPS are extracted from sludge, they are also likely to contain these complex chemical constituents. Moreover, from an application perspective, the identification of three PCs also provides a reliable framework for clarifying the thermal behaviour of EPS and guiding further studies on their decomposition mechanisms.

3.4. Temperature-dependent FTIR spectra from gaseous products and char residues

3.4.1. Gaseous products

The two-dimensional graphs of temperature-dependent FTIR spectra of gases released from the decomposition of EPS are shown in Fig. 2a1-b1. Various gases are released during the decomposition of EPS at temperatures ranging from 100 to 700 °C. However, only CH_4 (at around 3000–2880 cm^{-1}) and CO_2 (at 2365 and 668 cm^{-1}) show significant intensities, indicating that the main reaction during EPS decomposition is related to the release of these gases, such as decarboxylation, cracking, and demethylation (Zong et al., 2020). The temperature-dependent changes in gas-release intensity follow a comparable pattern, indicating that AS and BS have a similar decomposition mechanism; however, the quantity of gas evolved differs between the two samples. To determine the roles of each PC in the gases and the possible decomposition mechanism pathway of EPS, nine gases are selected including H_2O,–OH (3736 cm^{-1}), CH_4 (2930 cm^{-1}), CO_2 (2363 cm^{-1}, and 667 cm^{-1}), C=O (1761 cm^{-1}), C=C (1651 cm^{-1}), C-O (1161 cm^{-1}), NH_3 (996 cm^{-1}), HCN (716 cm^{-1}), HNCO (2281 cm^{-1}) (Jia et al., 2024; Zong et al., 2020). The corresponding GS curves for each gas were extracted from the 2D TG–FTIR spectra and analysed through Gaussian deconvolution, as illustrated in Fig. 2a2-11 and b2-11.as similar to DTG, each GS profile was also deconvoluted into several PC. Similarly to the DTG analysis, each GS profile was also deconvoluted into several PCs using the same Gaussian fitting procedure. Each GS-derived PC corresponds to a specific stage of gas evolution during thermal decomposition. By comparing the temperature ranges of the PCs obtained from the GS curves with those identified from the DTG curves, the gaseous species associated with each pseudo-component were determined. This cross-correlation enabled the assignment of characteristic evolved gases to individual thermal degradation stages. Furthermore, the attribution of DTG-derived pseudo-components was strengthened by integrating the AE results. The consistency among (i) DTG deconvolution, (ii) GS gas-evolution profiles, and (iii) kinetic parameters provides multi-parameter validation of the proposed pseudo-component identification.

Before the primary decomposition stages of EPS, new peaks (green line) in the GS graphs of H_2O, C=O from ketones, carboxylic acids, aldehyde, amides, and C=C from aromatic species are observed at around 107–110 °C, attributed to the degradation of moisture and light organic matter within the EPS matrix. The weaker peak intensity for BS compared with AS indicates less gas evolution in this stage. At 150 °C, CO_2 and NHCO, associated with the formation of nitrogen-containing species, are involved, followed by CH_4 at 200 °C. The emission of these gases is first governed by the decomposition of PC1, which has a peak temperature of < 250 °C.

The PC2 represents the dominant decomposition phase of EPS at 210–450 °C, where the evolution of all major gaseous species intensifies. Strong absorbance peaks for H_2O/–OH, CO_2, CH_4, C=O, C-O, HCN, and HNCO are observed within this temperature range of PC2. Amongst them, the PC2 and PC3 of GS graphs only contain C-O, NH_3, and HCN. The concurrent presence of HCN, HNCO, and NH_3 indicates the extensive degradation of proteinaceous and polypeptide backbones in EPS (e.g., peptidoglycans, amino acids), consistent with previous findings for biomass pyrolysis (Hu et al., 2025). The significant peak of CO_2 and CH_4 signify that demethylation and hydrocarbon-cracking reactions also proceed vigorously in this stage. This suggests the degradation of the aliphatic structure in EPS. Moreover, in comparison with other PCs, PC2 has the smallest peak at 250-350 °C for AS and 250–425 °C for BS in the GS curve of C=C generated from aromatic species, which is an overlapping evolution of PC2 and the initial part of PC3. The decomposition of PC3, occurring approximately between 300 and 600 °C, is characterised by the gradual release of CO_2, CH_4, and H_2O, indicating the progression of secondary cracking, decarboxylation, and dehydration reactions (Hu et al., 2025). The decreasing intensities of nitrogenous gases suggest the transformation of N-containing species into more

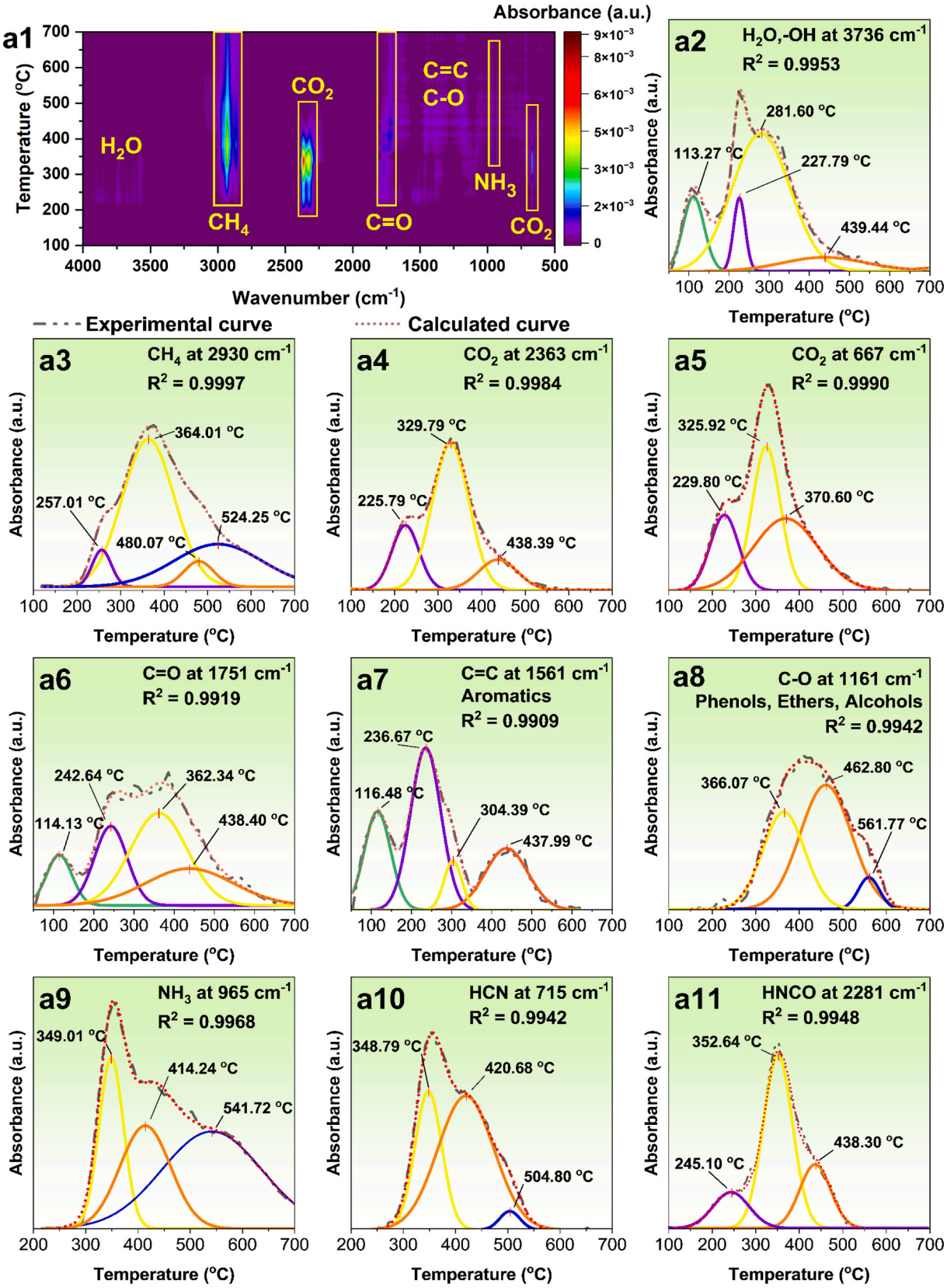

Fig. 2. The changes in FTIR spectra at various temperatures of gaseous products generated from AS (a) and BS (b). Purple line (< 250 °C): reaction related to PC1, yellow line (< 370 °C): reaction associated with PC2, orange line (<500 °C): reaction related to PC3, other lines: other reactions.

stable heteroaromatic structures. These findings are consistent with TG-FTIR analyses of humic substances, which exhibit comparable gas-evolution behaviour within 400–600 °C, corresponding to condensation and polyaromatic ring growth (Li et al., 2020). Similarly, previous

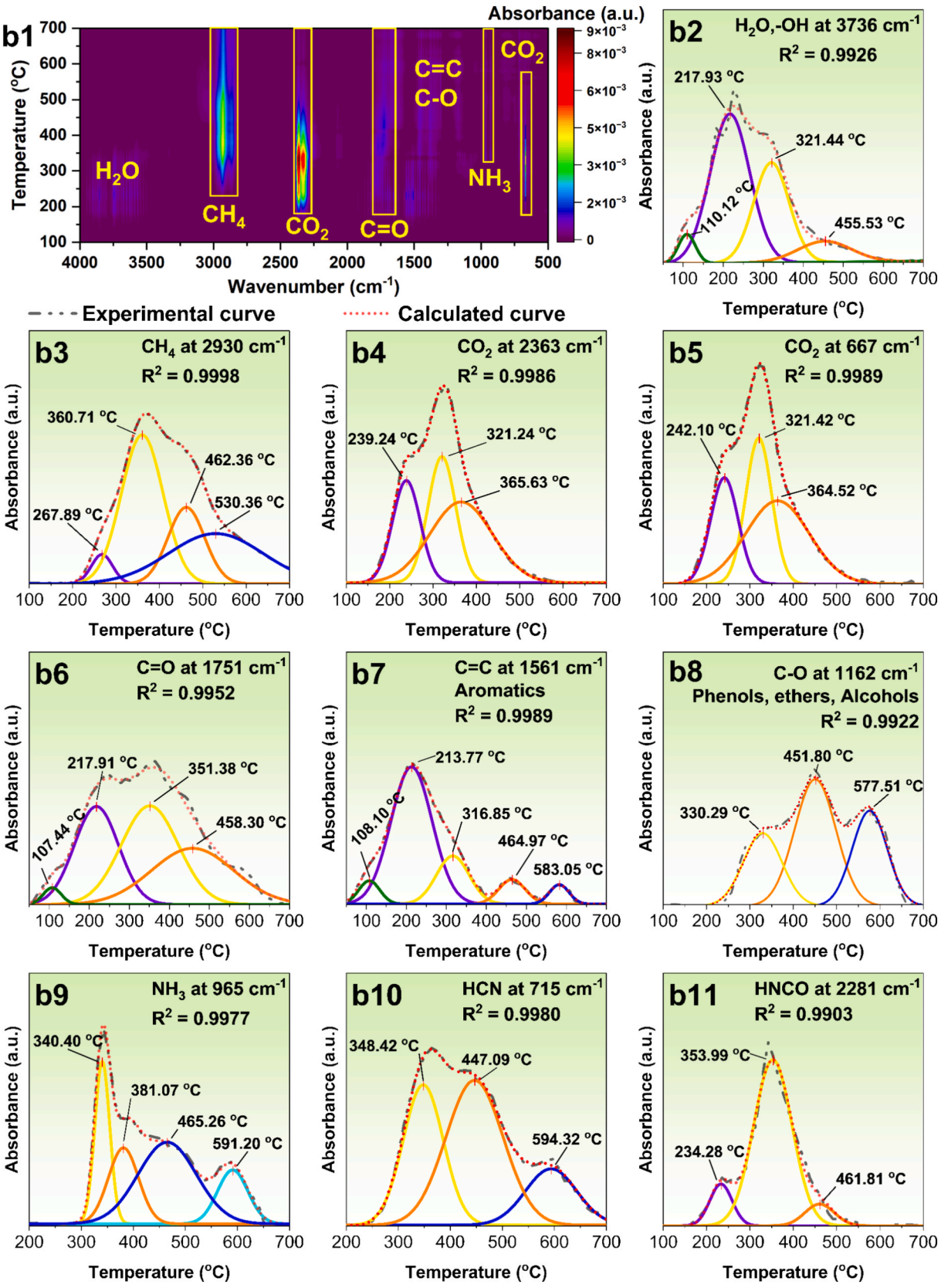

Fig. 2. (*continued*).

studies on sludge pyrolysis have attributed this high-temperature mass loss and gas composition to the degradation of refractory aromatic fractions and the structural rearrangement of char (Messaoudi et al., 2024). Notably, unexpected deconvolution peaks of HCN, NH_3, C-O, and CH_4 are detected in the GS curves above 500 °C for both EPS types, along with a distinctive C=C peak at 583 °C observed only in BS. This suggests

that secondary pyrolysis of some decomposition products occurs at elevated temperatures, where the aromatic char structure of BS may also be degraded. According to Jukka et al. (Leppälahti and Koljonen, 1995), the formation of HCN at such temperatures can be associated with the scission of cyano-aromatic compounds initially formed at lower temperatures. Hence, PC3 represents the final stabilisation pathway, dominated by carbonisation and aromatic cross-linking that yields a thermally stable char matrix.

3.4.2. Char residues

A fundamental understanding of the condensed-phase residue forming mechanisms is critical for elucidating the inherent charring capacity of EPS and a role of constituent biopolymers(Ula et al., 2025). In this study, the FTIR spectra of EPS residues obtained after TGA

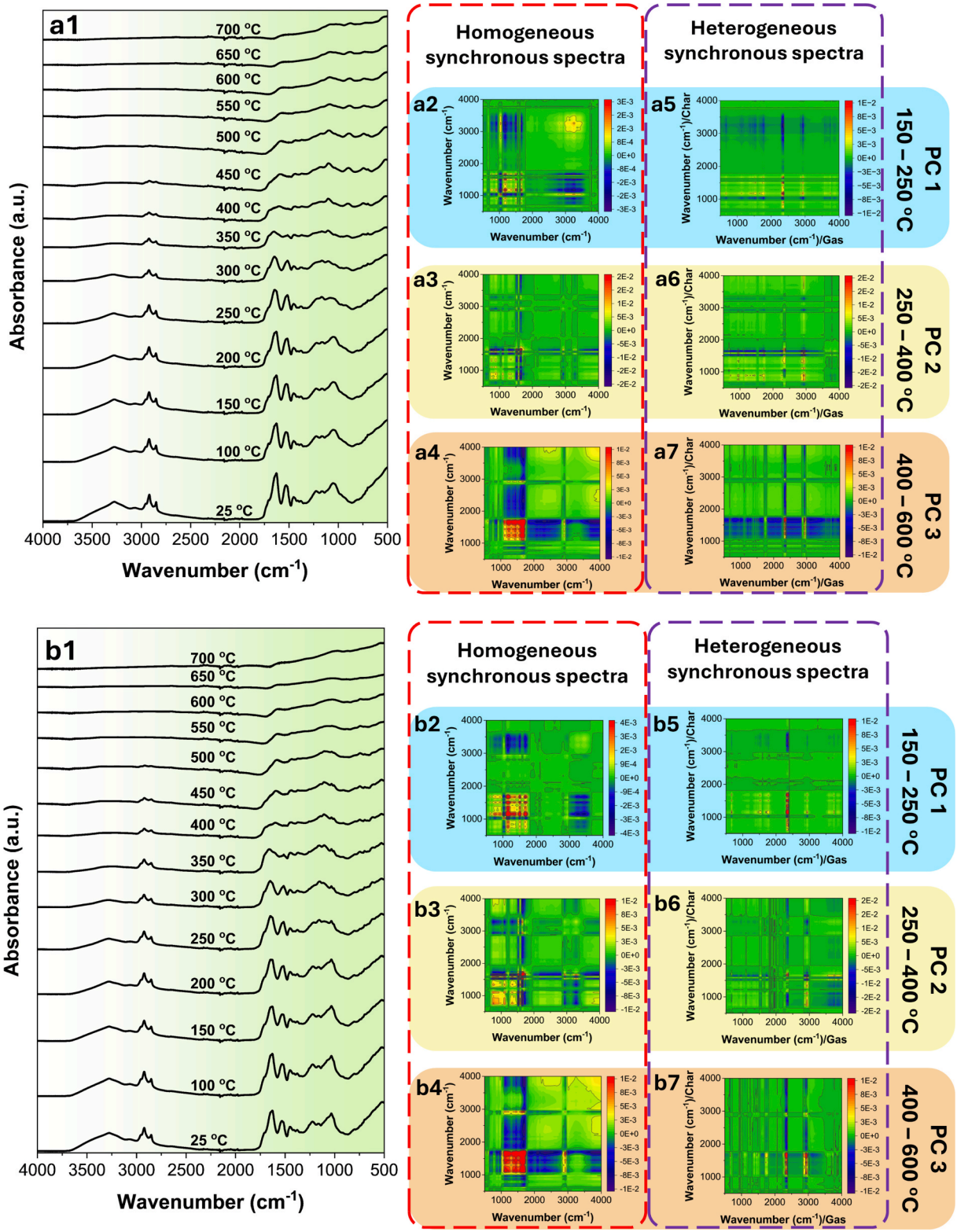

Fig. 3. The FTIR spectra of char residues from the decomposition reaction of AS (a1) and BS (b1) at different temperatures and their 2D-COS analysis (a2-b7).

measurements at different temperatures are analysed to investigate chemical evolution of solid phase. In general, the FTIR spectrum of EPS, Fig. 3, exhibits a characteristic peak at 3600 cm^{-1} to 3200 cm^{-1}, representing the stretching vibrations of the –OH and –NH groups, respectively. The bands at 2850 cm^{-1} and 2920 cm^{-1} correspond to the $–CH_2$ and $–CH_3$ symmetrical and asymmetrical stretching vibrations (Le et al., 2023). The protein structure in EPS can be characterised by amide I band at 1620 – 1720 cm^{-1} (C=O and –NH stretching), amide II bands at 1510 – 1530 cm^{-1} (C–H and N–H stretching) (Mishra et al., 2023), and amide III at 1210 cm^{-1} (C-N stretching) (Li et al., 2022). The peak at 1027 cm^{-1} corresponds to the C-O-C/P-O-P plane bending group of polysaccharides (Shi et al., 2023).

The char formation of multi-component materials such as EPS is a complex process involving various reactions, including cracking, depolymerisation, carbonisation, and condensation. However, the changes in functional groups observed from FTIR are not sufficient to fully characterise the char formation. FTIR spectra of char residues from the pyrolysis of EPS are shown in Fig. 3a2–7 and b2–7. The synchronous maps (Fig. 3a2–4 and b2–4) indicate the most susceptible functional groups of EPS under progressive heating. In contrast, the heterogeneous synchronous maps reveal correlations between the release of gaseous products and char formation, as gases are produced during the decomposition of char residues at different temperatures. Unlike the homogeneous 2D-COS, the diagonal positions in the hetero-synchronous spectra are not significant due to the different physical properties of the two phases (Chen et al., 2024). In theory, when gas species are released, the corresponding functional groups responsible for their evolution decrease, leading to a negative correlation between these functional groups in the char residues and the gaseous products. Conversely, gas release can also generate free radicals, which promote repolymerisation or carbonisation within the char residues, thereby enriching the carbon structure. In such cases, the gas release may exhibit a positive correlation with the functional groups in the char residues. From these simultaneous and competitive reactions, the char structure is progressively formed. Furthermore, it should be noted that the temperature ranges of each PC in this section differ slightly from those obtained from DTG deconvolution, as the overlapping temperature regions among components were intentionally reduced for clarity. Overall, the homogeneous synchronous spectra of both EPS samples exhibit similar patterns, indicating comparable char-formation mechanisms.

As observed from the FTIR spectra, no substantial structural changes are detected in the temperature range of 25–150 °C, suggesting that the release of low-molecular-weight volatiles does not significantly affect the overall chemical structure of EPS. The synchronous maps within the temperature range of 150–250 °C (Fig. 3a2 and b2) reveal several prominent auto-peaks at 912 cm^{-1} (C–H vibration of aromatic structures), 1024 cm^{-1} (C-O-C/P-O-P stretching in ethers and phosphates), 1172 cm^{-1} (C-N of amides and amines), 1508 cm^{-1} (C=C of aromatics), 1683 cm^{-1} (C=O of ketones, aldehydes, and acids), and 3100 cm^{-1} (–OH and N–H groups) (Zhang et al., 2025). The higher intensities of the synchronous peaks in the range of 600–1800 cm^{-1} in BS compared with AS indicate stronger reactions of these functional groups within this temperature interval. However, AS exhibits higher intensity at 3000–3500 cm^{-1} in the synchronous maps than BS, particularly due to the decrease in –OH groups in the char residues resulting from the dehydration reaction. The homogeneous synchronous maps of both EPS samples also show negative correlations between the 3100 cm^{-1} (–OH) and 1024 cm^{-1} (C–O–C groups) with other groups at 912 cm^{-1}, 1172 cm^{-1}, 1508 cm^{-1}, and 1683 cm^{-1}, implying that these functional groups change in opposite directions. In the heterogeneous maps, the O–H and C–O–C groups of the char residues exhibit negative correlations with most gas-release bands in this temperature region, indicating that the reactions are primarily driven by the decomposition of these oxygen-containing groups. Based on the literature, these observations suggest the formation of intermediate products, such as levoglucosenone, during the decomposition of polysaccharides through dehydration (Yang et al., 2020). On the other hand, CO_2 shows positive correlations with bands at 1000–1750 and 600–900 cm^{-1}, suggesting that decarboxylation and cleavage of oxygenated linkages (e.g., P-O-C/C-O-C) contribute to char formation during the decomposition of PC1, which is similar to the general decomposition of cellulose (Yang et al., 2020), hemicellulose (Shen et al., 2010), and chitin (Cabrera-Barjas et al., 2023).

Significant structural transformations of EPS occur in the temperature range of 250–400 °C. In the synchronous maps, the major auto-peaks for both EPS samples are observed at 600–900 cm^{-1} and 1024 cm^{-1}, as well as at the amide I (1643 cm^{-1}) and amide II (1519 cm^{-1}) bands. The bands at 1643 and 1519 cm^{-1} display negative correlations with most gaseous products in this temperature region (Fig. 3a6 and b6), indicating that the reactions are primarily associated with the decomposition of protein-derived structures. Moreover, these functional groups (1643 and 1519 cm^{-1}) show strong negative correlations with carbon-based groups (e.g., C–H and C–C), suggesting that the degradation of nitrogen-containing moieties promotes the formation of carbonaceous structures through N–C cross-linking within the developing char matrix. Conversely, CO_2 and CH_4 exhibit positive correlations with the bands at 1614 cm^{-1}, 600–900 cm^{-1}, and 1251 cm^{-1}, implying that decarboxylation and dehydrogenation reactions contribute to gas evolution and progressive char aromatisation. Notably, the 600–900 cm^{-1} region in the FTIR spectra shows pronounced changes, where a new absorption band near 900 cm^{-1} emerges between 350 and 400 °C, corresponding to C–H out-of-plane bending in aromatic rings. This marks the onset of aromatisation and the development of thermally stable char. The simultaneous attenuation of aliphatic –CH bands and enhancement of aromatic CH signals further support a Diels–Alder-type condensation mechanism (Yang et al., 2019). In addition, the sharpening of the 1083 cm^{-1} band indicates the formation of P–O–P linkages, consistent with our previous findings (Kim et al., 2022; Le et al., 2025b).

The final temperature stage occurs when the evolution of gaseous products gradually decreases. In this context, the decomposition of EPS is evidenced by the disappearance of absorption bands at 3500 cm^{-1}, 2900 cm^{-1}, and 1500 cm^{-1}, corresponding to O–H, C–H, and C=C stretching vibrations, respectively, as well as by the weakening of O=P–O–C bands at 1305 cm^{-1}, 1034 cm^{-1}, and 823 cm^{-1}, indicating progressive degradation of phosphate-containing groups. Most of the biochars exhibit intensified bands in the range of 1400–1600 cm^{-1}, attributed to aromatic C=C stretching (Zhang et al., 2025). Also in this temperature range, both EPS samples exhibit a major auto-peak in the homogeneous synchronous maps between 1000 cm^{-1} and 1800 cm^{-1}, mainly associated with aromatic and amide-related functional groups. In the heterogeneous maps, CH_4 and CO_2 display positive correlations with the functional groups in the 1000–1800 cm^{-1} region, indicating the degradation of residual aromatic structures, such as humic-like substances. Notably, AS shows strong negative correlations with most gaseous species, whereas BS exhibits the opposite trend. By comparing these results with the gas-release profiles (Fig. 1), it is observed that gas evolution gradually decreases within this temperature range. This indicates that the char derived from AS is more thermally stable, leading to suppressed gas evolution, which is consistent with the enhanced contribution of PC3 during this stage. In contrast, the functional groups of BS display positive correlations with most gaseous products, suggesting continuous thermal degradation. In the FTIR spectra, at approximately 500 °C, the spectra of the char residues from both AS and BS remain largely unchanged, signifying the formation of a stable carbonaceous matrix. Beyond 600 °C, a noticeable reduction in intensity within the 650–1000 cm^{-1} region for BS suggests slightly lower thermal stability compared with AS, whose char retains structural integrity up to around 700 °C. These findings explain the higher char yield observed for AS relative to BS.

4. Discussion

4.1. Interpretation of EPS's pseudo-components to their constitution and primary decomposition pathways

Using TG-FTIR combined with Gaussian deconvolution successfully distinguished the decomposition of EPS into three pseudo-components (PCs), each corresponding to specific organic fractions and reaction pathways. Due to the similar decomposition mechanism are demonstrated in the previous section, the primary decomposition pathways of EPS are reported as shown in Fig. 4.

According to Shen et al. (Shen et al., 2010), the decomposition of xylan mainly occurs between 200 °C and 350 °C, releasing H_2O, CO_2, and CH_4, a behaviour consistent with that observed for PC1. Due to their pentose-sugar structure, xylan tends to yield more char residue than cellulose, and its apparent activation energy increases with the degree of conversion (Qiao et al., 2019). The presence of HNCO, and NH_3 during this stage can be attributed to the decomposition of hetero-polysaccharides, such as lipopolysaccharides, which have been identified in EPS extracted from activated sludge by Li et al. (Li et al., 2024). Although the thermal behaviour of lipopolysaccharides has not yet been widely reported, the decomposition of phosphorylated chitin (Cabrera-Barjas et al., 2023)—a compound with a similar backbone structure—occurs within 200–350 °C, with an average activation energy of 125–145 kJ/mol. In addition, the evolution of volatile species, such as C=C, C=O, and C–C, indicates the simultaneous degradation of minor organic constituents (Zheng et al., 2025). Consequently, the possible reaction pathways of PC1 within this temperature range are proposed as Pathway I (Fig. 4).

In this context, the strong release of HNCO, NH_3, HCN, and CO_2, along with the attenuation of amide bands in the char residues between 200 and 450 °C, confirms peptide-bond cleavage and deamination as the primary mechanisms, corresponding to the breakdown of the proteinaceous structure. Zong et al. (Zong et al., 2020) reported that soybean proteins decompose at peak temperatures of 320 – 330 °C, with an average activation energy of 184 kJ/mol, accompanied by NH_3 release over 250 – 560 °C. A strong CH_4 signal is also observed in this temperature range, likely due to the degradation of lipids. According to Che et al. (Che et al., 2022), the mixture of proteins and lipids in sludge exhibits a higher activation energy (125 kJ/mol, FWO method) than protein alone (72.53 kJ/mol), which is attributed to the formation of small-molecule intermediates from lipid decomposition that hinders protein breakdown. This behaviour explains the relatively high activation energy of PC2 at conversion rates of 0.1–0.5, compared with PC1 in both cases of EPS. The corresponding decomposition pathways for PC2 are proposed as Pathways II and III (Fig. 4).

PC3, extending from 300 to 600 °C, exhibits the highest average activation energies (>180 kJ/mol) and is associated with the degradation of aromatic structures derived from humic-like substances (Pathways IV) and the condensation of char formed during PC1 and PC2. The decomposition of humic-like substances is evidenced by the evolution of C=C and C=O, as well as CO_2, CH_4, and –OH, due to cracking, decarboxylation, aromatisation, and dehydration reactions (Cheng et al., 2025). According to Yuan et al., 2022a, the recalcitrant and condensed nature of humic-like substances is due to their high aromatic structure, resulting in the highest activation energy of PC3 compared to others. Below 400 °C, the aromatic structures decompose into CO_2 and carbon-based syngas, while at temperatures above 450 °C, a small fraction of

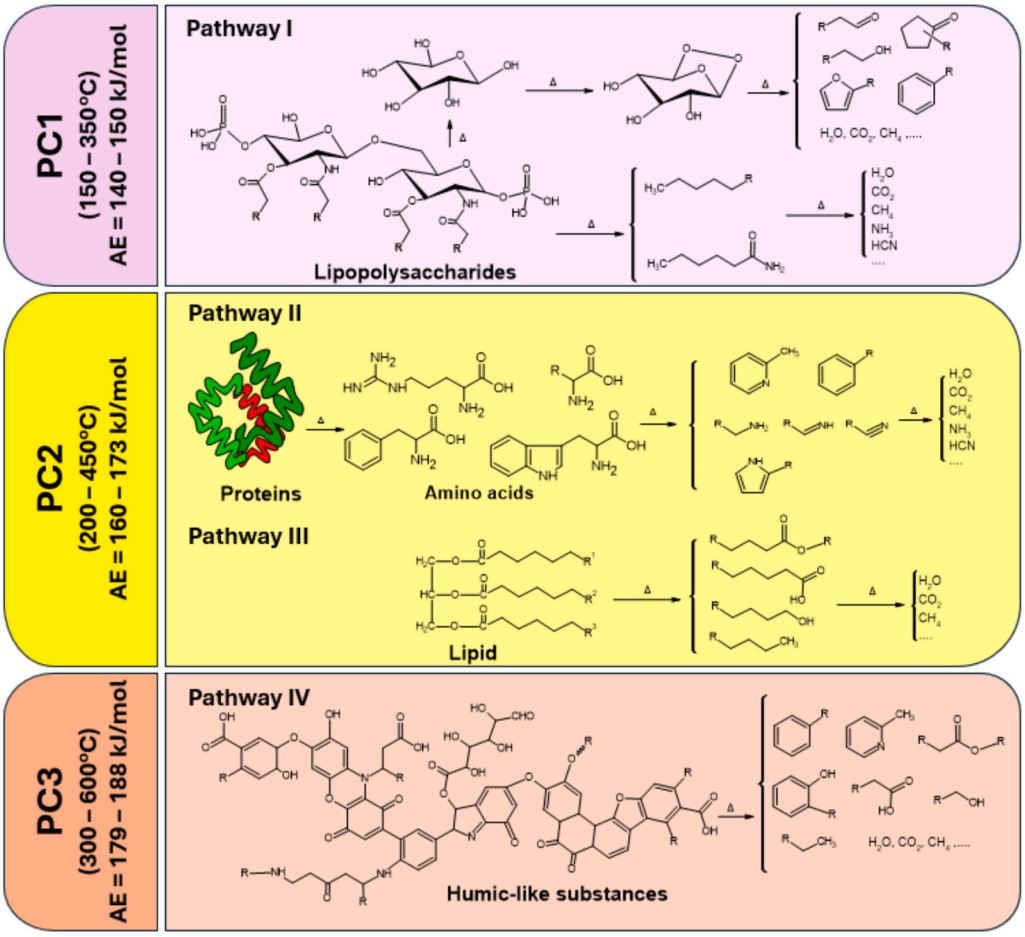

Fig. 4. Possible primary decomposition pathways of EPS's pseudo-components.

aromatics dissociates from the carbon matrix, resulting in the release of hydrocarbon gases (Guo et al., 2020). Meanwhile, residual lipids likely undergo thermal condensation and cyclisation, contributing to char development (Yuan et al., 2022b). This is supported by the observed transformation of C–H groups into C–O–C/P–O–C and C=C functionalities in the char residues (Zhuo et al., 2026).

5. Conclusions

This study provides insight into the pyrolysis behaviour and decomposition mechanisms of extracellular polymeric substances (EPS) recovered from wastewater sludge. By integrating TG–FTIR analysis with kinetic modelling, Gaussian deconvolution and 2D-COS analysis, the complex thermal evolution of EPS was resolved into three pseudo-components (PC1–PC3). PC1 was attributed to the decomposition of polysaccharides with low activation energy, PC2 to the breakdown of proteins and lipids, and PC3 to the transformation of aromatic compounds from humic-like substances and phosphorus-containing residues into a stable char. The progressive increase in activation energy across these stages confirmed the sequential transition from labile to recalcitrant structures. Comparative results between AS and BS revealed that AS exhibited lower AE at the onset but higher AE at the final stage, leading to enhanced char yield and thermal stability. The formation of a C-O-C/P-O-C and C=C groups within the char structure above 600 °C indicates strong potential for condensed-phase flame protection. These findings suggest that EPS, a waste-derived biopolymer, possibly possess inherent thermal resistance influenced by its natural C–N–P structure. This work provides preliminary mechanistic framework for exploring EPS as sustainable flame-retardant additives, contributing to both waste valorisation and fire-safe material design.

6. Declaration of generative AI use

During the preparation of this work, the author(s) used ChatGPT in order to improve clarity and grammar. After using this tool/service, the author(s) reviewed and edited the content as needed and take(s) full responsibility for the content of the publication.

CRediT authorship contribution statement

Tan Minh Le: Writing – review & editing, Writing – original draft, Visualization, Methodology, Investigation, Formal analysis, Conceptualization. **Yuemei Lin:** Writing – review & editing, Supervision, Methodology, Investigation, Conceptualization. **Wei-Qin Zhuang:** Methodology, Investigation. **Mark C.M. van Loosdrecht:** Writing – review & editing, Methodology, Investigation. **Krishnan Jayaraman:** Writing – review & editing, Supervision, Methodology, Investigation, Conceptualization. **Nam Kyeun Kim:** Writing – review & editing, Supervision, Project administration, Methodology, Investigation, Funding acquisition, Conceptualization.

Declaration of competing interest

The authors declare that they have no known competing financial interests or personal relationships that could have appeared to influence the work reported in this paper.

Acknowledgements

This research is supported by the Marsden Fund Council from Government funding (Fast-Start Fund, Grant number: MFP-UOA2218), administrated by the Royal Society Te Apārangi (New Zealand). We also acknowledge the support of materials from Watercare Service Limited in New Zealand. The authors would like to thank Dr. Cheng Wang and Prof. Guan Heng Yeoh from the School of Mechanical and Manufacturing Engineering, the University of New South Wales, Australia, for supporting the TG-FTIR measurement.

Appendix A. Supplementary data

Supplementary data to this article can be found online at https://doi.org/10.1016/j.wasman.2026.115518.

Data availability

Data will be made available on request.

References

Cabrera-Barjas, G., Jimenez, R., Romero, R., Valdes, O., Nesic, A., Hernández-García, R., Neira, A., Alejandro-Martín, S., de la Torre, A.F., 2023. Value-added long-chain aliphatic compounds obtained through pyrolysis of phosphorylated chitin. Int. J. Biol. Macromol. 238, 124130.

Campo, R., Carretti, E., Lubello, C., Lotti, T., 2022. Recovery of structural extracellular polymeric substances (sEPS) from aerobic granular sludge: Insights on biopolymers characterization and hydrogel properties for potential applications. J. Environ. Manage. 324, 116247.

Che, D., Wang, L., Liu, H., Sun, B., Guo, S., 2022. Effects of lipids on sludge and chlorella protein pyrolysis by thermogravimetry Fourier transform infrared spectrometry. J. Environ. Chem. Eng. 10, 107011.

Chen, X., Lee, Y.-J., Yuan, T., Lei, Z., Adachi, Y., Zhang, Z., Lin, Y., van Loosdrecht, M.C. M., 2022. A review on recovery of extracellular biopolymers from flocculent and granular activated sludges: Cognition, key influencing factors, applications, and challenges. Bioresour. Technol. 127854.

Chen, Z., Li, W., Huang, S., Zhuang, P., Jia, D., Evrendilek, F., Zhong, S., Ninomiya, Y., Yang, Z., He, Y., 2024. Dynamic, synergistic, and optimal emissions and kinetics of volatiles during co-pyrolysis of soil remediation plants with kaolin/modified kaolin. Chem. Eng. J. 483, 149214.

Cheng, P., Li, Z., Zheng, Y., Meng, Q., Yu, Y., Jin, Y., Gao, X., Guo, X., Jia, L., 2025. Study on the regulation of performance and Hg0 removal mechanism of MIL-101 (Fe)-derived carbon materials. Sep. Purif, Technol.

De Bruin, S., Riisgaard-Jensen, M., Hansen, S.H., Van Loosdrecht, M.C.M., Nielsen, P.H., Lin, Y., 2026. Global insights into extracellular polymeric substances from activated sludge: Yield, composition, and microbial communities. Water Res. 289, 124726. https://doi.org/10.1016/j.watres.2025.124726.

DuBois, M., Gilles, K.A., Hamilton, J.K., Rebers, P.A. t, Smith, F., 1956. Colorimetric method for determination of sugars and related substances. Anal. Chem. 28, 350–356.

Erickson, C.B., Ankenman, B.E., Sanchez, S.M., 2018. Comparison of Gaussian process modeling software. Eur. J. Oper. Res. 266, 179–192.

Felz, S., Al-Zuhairy, S., Aarstad, O.A., van Loosdrecht, M.C.M., Lin, Y.M., 2016. Extraction of structural extracellular polymeric substances from aerobic granular sludge. JoVE (J. Vis. Exp.), e54534.

Felz, S., Vermeulen, P., van Loosdrecht, M.C.M., Lin, Y.M., 2019. Chemical characterization methods for the analysis of structural extracellular polymeric substances (EPS). Water Res. 157, 201–208. https://doi.org/10.1016/j.watres.2019.03.068 WE - Science Citation Index Expanded (SCI-EXPANDED).

Frølund, B., Palmgren, R., Keiding, K., Nielsen, P.H., 1996. Extraction of extracellular polymers from activated sludge using a cation exchange resin. Water Res. 30, 1749–1758.

Gan, F., Wu, K., Ma, F., Wei, C., Du, C., 2022. In-situ monitoring of nitrate in industrial wastewater using Fourier transform infrared attenuated total reflectance spectroscopy (FTIR-ATR) coupled with chemometrics methods. Heliyon 8.

Gesese, T.N., Getahun, E., Getahun, A.A., 2024. Investigation of thermal degradation properties and chemical kinetic characteristics of biomass pyrolysis via TG/DTG and FTIR techniques: Sesame stalks as potential source of bioenergy in Ethiopia. Int. J. Energy Res. 2024, 8891126.

Guo, F., Qin, S., Xu, L., Bai, Y., Xing, B., 2020. Thermal degradation features of soil humic acid sub-fractions in pyrolytic treatment and their relation to molecular signatures. Sci. Total Environ. 749, 142318.

Hamed, H.B., Mainardis, M., Moretti, A., Toye, D., Léonard, A., 2025. Extracellular polymeric substances (EPS) in sewage sludge management: a call for methodological standardization. J. Environ. Manage. 376, 124407. https://doi.org/10.1016/j.jenvman.2025.124407.

Hu, Q., Zhang, Y., Luo, C., Mi, Y., Chen, M., Zheng, Y., Hu, Z., 2025. Pyrolysis of nitrogen-rich microalgae: kinetics, products, and amino acid contributions. Bioresour. Technol. 132899.

Jia, D., Liang, J., Liu, J., Chen, D., Evrendilek, F., Wen, T., Cao, H., Zhong, S., Yang, Z., He, Y., 2024. Insights into pyrolysis of ginger via TG-FTIR and Py-GC/MS analyses: Thermochemical behaviors, kinetics, evolved gas, and products. J. Anal. Appl. Pyrol. 179, 106442. https://doi.org/10.1016/J.JAAP.2024.106442.

Kim, N.K., Bhattacharyya, D., van Loosdrecht, M., Lin, Y., 2023. Enhancement of fire resistance and mechanical performance of polypropylene composites containing cellulose fibres and extracellular biopolymers from wastewater sludge. Polym. Test. 127, 108185.

Kim, N.K., Lin, R., Bhattacharyya, D., van Loosdrecht, M.C.M., Lin, Y., 2022. Insight on how biopolymers recovered from aerobic granular wastewater sludge can reduce the flammability of synthetic polymers. Sci. Total Environ. 805, 150434.

Lasch, P., Noda, I., 2019. Two-dimensional correlation spectroscopy (2D-COS) for analysis of spatially resolved vibrational spectra. Appl. Spectrosc. 73, 359–379.
Le, T.M., Lin, Y., Zhuang, W.-Q., Jayaraman, K., Kim, N.K., 2025a. Effects of Extraction Methods on the thermal Stability of Extracellular Polymeric Substances-based Biomaterials from Wastewater Sludge. Environ. Sci. Technol. https://doi.org/10.1021/acs.est.4c10329.
Le, T.M., Lin, Y., Zhuang, W.-Q., van Loosdrecht, M.C.M., Jayaraman, K., Kim, N.K., 2025b. Unlocking the potential flame-retardant mechanisms of extracellular polymeric substances recovered from municipal sludge. J. Environ. Chem. Eng. 13, 117907. https://doi.org/10.1016/j.jece.2025.117907.
Le, T.M., Tran, C.L., Nguyen, T.X., Duong, Y.H.P., Le, P.K., Tran, V.T., 2023. Green preparation of chitin and nanochitin from black soldier fly for production of biodegradable packaging material. J. Polym. Environ. 1–12.
Leppälahti, J., Koljonen, T., 1995. Nitrogen evolution from coal, peat and wood during gasification: Literature review. Fuel Process. Technol. 43, 1–45.
Li, J., Hao, X., Gan, W., van Loosdrecht, M.C.M., Wu, Y., 2022. Controlling factors and involved mechanisms on forming alginate like extracellular polymers in flocculent sludge. Chem. Eng. J. 439, 135792.
Li, J., Hao, X., Persiani, R., van Loosdrecht, M.C.M., Lin, Y., 2024. Reinvestigating the composition of alginate-like exopolymers extracted from activated sludge. ACS ES&T Water 4, 3007–3015.
Li, T., Song, F., Zhang, J., Liu, S., Xing, B., Bai, Y., 2020. Pyrolysis characteristics of soil humic substances using TG-FTIR-MS combined with kinetic models. Sci. Total Environ. 698, 134237.
Li, X., Lin, S., Hao, T., Khanal, S.K., Chen, G., 2019. Elucidating pyrolysis behaviour of activated sludge in granular and flocculent form: reaction kinetics and mechanism. Water Res. 162, 409–419.
Liang, D., Zhu, X., Dai, P., Lu, X., Guo, H., Que, H., Wang, D., He, T., Xu, C., Robin, H.M., 2021. Preparation of a novel lignin-based flame retardant for epoxy resin. Mater. Chem. Phys. 259, 124101.
Lin, Y., Liao, Y., Yu, Z., Fang, S., Ma, X., 2017. A study on co-pyrolysis of bagasse and sewage sludge using TG-FTIR and Py-GC/MS. Energy Convers. Manag. 151, 190–198.
Lin, Y.M., Nierop, K.G.J., Girbal-Neuhauser, E., Adriaanse, M., Van Loosdrecht, M.C.M., 2015. Sustainable polysaccharide-based biomaterial recovered from waste aerobic granular sludge as a surface coating material. Sustain. Mater. Technol. 4, 24–29.
Messaoudi, H., Koukouch, A., Bakhattar, I., Asbik, M., Bonnamy, S., Bennouna, E.G., Boushaki, T., Sarh, B., Rouboa, A., 2024. Physicochemical characterization, thermal behavior, and pyrolysis kinetics of sewage sludge. Energies (basel). 17, 582.
Mishra, A., Jung, D., Kim, N.K., Bhattacharyya, D., 2023. Influence of chicken feather fibre processing technique on mechanical and fire performances of flame-retardant polypropylene composites. Compos. A Appl. Sci. Manuf. 165, 107338.
Morgan, J.W., Forster, C.F., Evison, L., 1990. A comparative study of the nature of biopolymers extracted from anaerobic and activated sludges. Water Res. 24, 743–750. https://doi.org/10.1016/0043-1354(90)90030-A.
Mu, X., Jin, Z., Chu, F., Cai, W., Zhu, Y., Yu, B., Song, L., Hu, Y., 2022. High-performance flame-retardant polycarbonate composites: mechanisms investigation and fire-safety evaluation systems establishment. Compos. B Eng. 238, 109873.
Ni, Z., Song, Z., Bi, H., Jiang, C., Sun, H., Qiu, Z., He, L., Lin, Q., 2023. The effect of cellulose on the combustion characteristics of coal slime: TG-FTIR, principal component analysis, and 2D-COS. Fuel 333, 126310. https://doi.org/10.1016/J.FUEL.2022.126310.
Nkuna, S.G., Olwal, T.O., Chowdhury, S.D., Ndambuki, J.M., 2024. A review of wastewater sludge-to-energy generation focused on thermochemical technologies: an improved technological, economical and socio-environmental aspect. Cleaner Waste Syst. 7, 100130. https://doi.org/10.1016/J.CLWAS.2024.100130.
Park, Y., Jin, S., Noda, I., Jung, Y.M., 2018. Recent progresses in two-dimensional correlation spectroscopy (2D-COS). J. Mol. Struct. https://doi.org/10.1016/j.molstruc.2018.04.099.
Qiao, Y., Wang, B., Ji, Y., Xu, F., Zong, P., Zhang, J., Tian, Y., 2019. Thermal decomposition of castor oil, corn starch, soy protein, lignin, xylan, and cellulose during fast pyrolysis. Bioresour. Technol. 278, 287–295.
Shen, D.K., Gu, S., Bridgwater, A.V., 2010. Study on the pyrolytic behaviour of xylan-based hemicellulose using TG–FTIR and Py–GC–FTIR. J. Anal. Appl. Pyrol. 87, 199–206.
Shi, C., Zeng, R.-G., Hao, L.-T., Hao, X.-D., Li, J., 2023. Extracting compositional blocks of alginate-like extracellular polymers (ALE) from conventional activated sludge (CAS). Sci. Total Environ. 867, 161371.
Song, F., Li, T., Zhang, J., Wang, X., Bai, Y., Giesy, J.P., Xing, B., Wu, F., 2019. Novel insights into the kinetics, evolved gases, and mechanisms for biomass (sugar cane residue) pyrolysis. Environ. Sci. Technol. 53, 13495–13505.
Song, G., Zhao, S., Zhao, K., Liu, R., Hu, C., van Loosdrecht, M.C.M., 2026. Recovery of C, N, and P from waste activated sludge by enzymatic anaerobic fermentation: Stoichiometry and metatranscriptomics analysis. Resour. Conserv. Recycl. 225, 108578.
Thipkhunthod, P., Meeyoo, V., Rangsunvigit, P., Rirksomboon, T., 2007. Describing sewage sludge pyrolysis kinetics by a combination of biomass fractions decomposition. J. Anal. Appl. Pyrol. 79, 78–85. https://doi.org/10.1016/J.JAAP.2006.10.005.
Tobar, F., Robert, A., Silva, J.F., 2023. Gaussian process deconvolution. Proc. R. Soc. A 479, 20220648.
Uchimiya, M., Noda, I., Orlov, A., Ramakrishnan, G., 2018. In situ and ex situ 2D infrared/fluorescence correlation monitoring of surface functionality and electron density of biochars. ACS Sustain. Chem. Eng. 6, 8055–8062.
Ula, N.M., Le, T.M., Lin, Y., van Loosdrecht, M.C.M., Bhattacharyya, D., Jayaraman, K., Kim, N.K., 2025. Flammability and mechanical performance of fibreboards based on wool fibres and extracellular polymeric substances recovered from wastewater sludge. Mater. Today Sustainability 101210.
Vyazovkin, S., 2025. Correlation between activation energy and reaction temperature as observed in thermal analysis kinetics. Thermochim Acta 743, 179911.
Vyazovkin, S., Burnham, A.K., Criado, J.M., Pérez-Maqueda, L.A., Popescu, C., Sbirrazzuoli, N., 2011. ICTAC Kinetics Committee recommendations for performing kinetic computations on thermal analysis data. Thermochim Acta 520, 1–19.
Wang, Z., Che, Y., Li, J., Wu, W., Yan, B., Zhang, Y., Wang, X., Yu, F., Chen, G., Zuo, X., 2022. Effects of anaerobic digestion pretreatment on the pyrolysis of Sargassum: Investigation by TG-FTIR and Py-GC/MS. Energy Convers. Manag. 267, 115934.
Yang, C., Li, R., Zhang, B., Qiu, Q., Wang, B., Yang, H., Ding, Y., Wang, C., 2019. Pyrolysis of microalgae: a critical review. Fuel Process. Technol. 186, 53–72.
Yang, H., Gong, M., Hu, J., Liu, B., Chen, Y., Xiao, J., Li, S., Dong, Z., Chen, H., 2020. Cellulose pyrolysis mechanism based on functional group evolutions by two-dimensional perturbation correlation infrared spectroscopy. Energy Fuel 34, 3412–3421.
Yuan, Z., Luo, J., Ndudi, E.A., Ma, W., Zhu, N., Lou, Z., 2022a. Systematic understanding of char-volatile evolution and interaction mechanism during sewage sludge pyrolysis through in-situ tracking solid-state reaction and products fate. J. Hazard. Mater. 432, 128669.
Yuan, Z., Zhou, Z., Luo, J., Yuan, H., Zhu, N., Lou, Z., 2022b. Quantifying the thermochemical pathways of soluble organics in sewage sludge flocs during pyrolysis for precursor optimization and by-product control. Chem. Eng. J. 444, 136627.
Zeng, Y., Liu, Z., Yu, J., Hu, E., Jia, X., Tian, Y., Wang, C., 2024. Pyrolysis kinetics and characteristics of waste tyres: Products distribution and optimization via TG-FTIR-MS and rapid infrared heating techniques. Chem. Eng. J. 482, 149106. https://doi.org/10.1016/J.CEJ.2024.149106.
Zhang, X., Xu, Z., Sun, Y., Mohanty, S.K., Lei, H., Khan, E., Tsang, D.C.W., 2025. Implications of Pyrolytic Gas Dynamic Evolution on Dissolved Black Carbon Formed During Production of Biochar from Nitrogen-Rich Feedstock. Environ. Sci. Technol.
Zheng, M., Hu, Z., Liu, T., Sperandio, M., Volcke, E.I.P., Wang, Z., Hao, X., Duan, H., Vlaeminck, S.E., Xu, K., 2024. Pathways to advanced resource recovery from sewage. Nat. Sustain. 1–10.
Zheng, Y., Cheng, P., Li, Z., Fan, C., Wen, J., Yu, Y., Jia, L., 2025. Efficient removal of gaseous elemental mercury by Fe-UiO-66@ BC composite adsorbent: Performance evaluation and mechanistic elucidation. Sep. Purif. Technol. 372, 133463.
Zhu, F.L., Li, X., Feng, Q.Q., 2021. Thermal decomposed behavior and kinetic study for untreated and flame retardant treated regenerated cellulose fibers using thermogravimetric analysis. J. Therm. Anal. Calorim. 145, 423–435.
Zhuo, J., Wang, X., Sheng, N., Yao, X., Sun, J., Tao, X., Zhao, L., Sha, J., 2026. Dual-activation with oyster shell: Synergistic engineering of N/P co-doped hierarchical porous carbon from intumescent flame retardants for high-performance dual-ion batteries. J. Energy Storage 150, 120481.
Zong, P., Jiang, Y., Tian, Y., Li, J., Yuan, M., Ji, Y., Chen, M., Li, D., Qiao, Y., 2020. Pyrolysis behavior and product distributions of biomass six group components: Starch, cellulose, hemicellulose, lignin, protein and oil. Energy Convers. Manag. 216, 112777.